

The Consistency of MJO Teleconnection Patterns: An Explanation Using Linear Rossby Wave Theory

KAI-CHIH TSENG, ERIC MALONEY, AND ELIZABETH BARNES

Colorado State University, Fort Collins, Colorado

(Manuscript received 6 April 2018, in final form 30 October 2018)

ABSTRACT

The Madden–Julian oscillation (MJO) excites strong variations in extratropical atmospheric circulations that have important implications for subseasonal-to-seasonal (S2S) prediction. A previous study showed that particular MJO phases are characterized by a consistent modulation of geopotential heights in the North Pacific and adjacent regions across different MJO events, and demonstrated that this consistency is beneficial for extended numerical weather forecasts (i.e., lead times of two weeks to one month). In this study, we examine the physical mechanisms that lead some MJO phases to have more consistent teleconnections than others using a linear baroclinic model. The results show that MJO phases 2, 3, 6, and 7 consistently generate Pacific–North American (PNA)-like patterns on S2S time scales while other phases do not. A Rossby wave source analysis is applied and shows that a dipole-like pattern of Rossby wave source on each side of the subtropical jet can increase the pattern consistency of teleconnections due to the constructive interference of similar teleconnection signals. On the other hand, symmetric patterns of Rossby wave source can dramatically reduce the pattern consistency due to destructive interference. A dipole-like Rossby wave source pattern is present most frequently when tropical heating is found in the Indian Ocean or the Pacific warm pool, and a symmetric Rossby wave source is present most frequently when tropical heating is located over the Maritime Continent. Thus, the MJO phase-dependent pattern consistency of teleconnections is a special case of this mechanism.

1. Introduction

The Madden–Julian oscillation (MJO) is one of the dominant modes of variability in the tropics, characterized by planetary-scale wavenumbers 1–3 and 30–90-day intraseasonal time scales (Madden and Julian 1971; Adames and Kim 2016). The MJO has profound impacts around the globe, including modulating the frequency of cyclone genesis in the North Atlantic and Pacific (Liebmann et al. 1994; Maloney and Hartmann 2000; Kim et al. 2008), influencing the timing of monsoon onset (Sui and Lau 1992; Lawrence and Webster 2002), and modulating Arctic surface air temperature (Yoo et al. 2012). A particular motivation for improving our knowledge of the MJO is that some persistent and devastating weather phenomena, such as blocking anticyclones and extratropical storms, are related to the low-frequency variability of geopotential height in the extratropics, which can be driven by tropical–extratropical teleconnections

(Henderson et al. 2016; Mundhenk et al. 2016). Further, the period of the MJO occurs on subseasonal to seasonal (S2S) time scales, a window with lower traditional prediction skill (Vitart 2017).

Since the 1980s, the mechanisms of tropical heating–induced extratropical responses have been extensively studied based on the knowledge of barotropic and baroclinic vorticity equations in spherical coordinates (Hoskins and Karoly 1981). Observational and numerical studies have also shown coherent variations between extratropical geopotential height anomalies and tropical heating (e.g., El Niño–Southern Oscillation; Bjerknes 1969; Simmons et al. 1983). A number of studies proposed mechanisms to explain the growth of the teleconnected signals such as the barotropic conversion by the heating–induced divergent wind in the upper troposphere (Simmons et al. 1983) or dynamical feedbacks between synoptic eddies and low-frequency modes of variability (Held et al. 1988; Jin et al. 2006). While most of the research mentioned above focused on stationary forcings (e.g., ENSO or topography) and the steady-state response, since the 1990s, scientists have been also

Corresponding author: Kai-Chih Tseng, kctsens@rams.colostate.edu

DOI: 10.1175/JCLI-D-18-0211.1

© 2018 American Meteorological Society. For information regarding reuse of this content and general copyright information, consult the [AMS Copyright Policy](https://www.ametsoc.org/PUBSReuseLicenses) (www.ametsoc.org/PUBSReuseLicenses).

investigating coherent variations between MJO convection and extratropical responses. By using objective analysis (e.g., lag regression between an MJO index and time-filtered extratropical streamfunction anomalies; Black 1997; Matthews et al. 2004) and idealized simulations based on the linearized barotropic vorticity equation forced by a propagating heating source (Ferranti et al. 1990), the most unstable modes [e.g., the Pacific–North American pattern (PNA) and North Atlantic Oscillation (NAO)] excited by the MJO in the extratropical regions were discovered. Mori and Watanabe (2008) conducted a detailed vorticity budget analysis showing that linear dynamics governed by the interaction between the mean state and intraseasonal variability dominates the growth and triggering mechanisms of the PNA. This process was further verified in an idealized simulation with linearized primitive equations (Seo and Lee 2017).

Recently, by using reanalysis data and ECMWF ensemble hindcasts, Tseng et al. (2018) found that MJO heating in specific phases (e.g., phases 2, 3, 6, and 7) generates consistent teleconnection patterns in the extratropical Pacific and North America from one event to the next. The pattern consistency was defined by examining the fraction of events with high pattern correlations of the 500-hPa geopotential height anomaly field. Their study further showed that the phases with consistent teleconnection patterns have improved numerical weather forecasts at 2–4-week lead times while the other phases are constrained by the traditional limit of midlatitude prediction skill (about 10 days; Hamill and Kiladis 2014). This result from Tseng et al. (2018) implies that if one can reveal the fundamental mechanisms that cause the phase-dependent pattern consistency of tropical–extratropical teleconnections, one might be able to determine why prediction skill improves in specific MJO phases.

Here, the mechanism responsible for the MJO phase-dependent pattern consistency of tropical–extratropical teleconnections is investigated by using a linear baroclinic model (LBM) and reanalysis data. This paper is organized as follows. In section 2, detailed descriptions of the LBM, data, and methods are provided. In section 3, the phase-dependent pattern consistency documented in Tseng et al. (2018) is interpreted through the LBM. It will be shown that the teleconnections during some MJO phases are less sensitive to variations in the basic state and variations in the MJO's heating pattern from event to event than others. In section 4, a mechanism is proposed to explain why the pattern consistency of MJO-induced teleconnections is a phase-dependent phenomenon. In section 5, the concept of teleconnection pattern consistency in response to tropical heating is generalized

beyond the MJO using reanalysis data. Section 6 holds the conclusions and remarks.

2. Data, model, and method

a. Linear baroclinic model

1) MODEL DESCRIPTION

In this study, a linear baroclinic model (Watanabe and Kimoto 2000) is used to examine the mechanisms of tropical–extratropical teleconnections. There are two main reasons for using an LBM. First, in a linearized model, it is easier to separate the anomalous response from basic state, which cannot be done in the real world or a model with feedback processes. Second, previous studies have shown that the MJO-induced teleconnection is dominated by linear dynamics (Mori and Watanabe 2008). In this study, we go one step further to see whether the phase-dependent teleconnection pattern consistency documented in Tseng et al. (2018) also exists in a linear model. If the phase-dependent pattern consistency can be simulated by the LBM, we can narrow down the possible mechanisms using dry and linear dynamical considerations.

In the LBM, the primitive equations are linearized about prescribed basic states. The vertical and horizontal resolutions of the model are 20 sigma levels and T42, respectively. For the numerical damping, we employed fourth-order biharmonic damping (∇^4) with an e -folding time of 2 h for the shortest wavenumber. We also employed Rayleigh friction and Newtonian cooling in the model with an e -folding time of 20 days in most model layers while the top two layers and the bottom three layers have e -folding times of 0.5 days. All of these settings are fixed over the different simulations to ensure that differences in the model output result from only the different forcing and basic states.

2) MODEL BASIC STATE AND MJO FORCING

When we use the LBM as the platform for mechanism testing, two inputs are required: a basic state and anomalous heating. In the LBM, the linear operator is associated with the given basic state pattern and the anomalous heating is used to drive the anomalous circulation in the model. For the model basic states, the European Centre for Medium-Range Weather Forecasts (ECMWF) third-generation reanalysis product (ERA-Interim; Dee et al. 2011) from 1979 to 2015 is used. ERA-Interim is provided on 20 vertical pressure levels from 1000 to 100 hPa and the horizontal resolution is interpolated to T42 resolution (approximately 2.8° grid spacing). Since the extratropical teleconnections

are stronger in boreal winter than in boreal summer, the necessary variables for the basic states are derived from extended boreal winter averages (November to March) during 1979 to 2015.

The daily mean apparent heat source Q_1 is computed following Yanai et al. (1973) for use in representing intraseasonal forcing (1). In (1), v is the horizontal wind, ω is the pressure velocity, and s is the dry static energy defined as $s = c_p T + gz$, where c_p is the specific heat, T is the temperature, g is the gravitational acceleration, and z is the height:

$$Q_1 \equiv \frac{\partial s}{\partial t} + v \cdot \nabla s + \omega \frac{\partial s}{\partial p}. \quad (1)$$

Following Yanai et al. (1973), the heat budget residual Q_1 represents subgrid-scale physical processes including radiative cooling, condensation heating, evaporation, and eddy heat flux convergence. In particular, in regions with active deep convection, Q_1 is dominated by deep convective heating. In this study, the anomalous Q_1 is derived by removing the linear trend and the first three harmonics of the seasonal cycle. Further, a Lanczos bandpass filter (20–100 days) with nine weights is applied to obtain the intraseasonal time scale diabatic heating anomaly Q'_1 . In addition, to ensure that all signals originate from the tropics rather than being excited by local heating anomalies in extratropical regions, we only specify model forcing between 30°S and 30°N.

3) EXPERIMENTAL DESIGN

To test the teleconnected response to the variations of basic states and MJO forcing, we conduct two sets of experiments in this study: 1) Fixed MJO heating (FixQ1 hereafter) and 2) Fixed basic state (FixBS hereafter). The main philosophy of these two experiments is to perform ensembles of simulations with small perturbations added either to the basic state or MJO heating to test the phase-dependent consistency of tropical–extratropical teleconnections when given these modest perturbations. In the FixQ1 experiment, we use the MJO-phase composited Q'_1 as the forcing. For the MJO event selection in this study, unless specified otherwise, an MJO event is retained if the OLR-based MJO index (OMI; see the section 2b for detailed descriptions; Kiladis et al. 2014) indicates the same phase for at least 5 consecutive days and the amplitude of the index meets or exceeds 1 standard deviation for all 5 days. FixQ1 gets its name because the MJO Q'_1 is fixed for each of the eight MJO phases while the basic state of the circulation and the static stability are varied. Specifically, we replace the model basic states with 36 different realizations. Each realization is derived from a different

years' boreal winter averaged including three-dimensional winds, temperature, specific humidity, and surface pressure (from 1979 to 2015). Thus, for each MJO phase, we have 36 different simulations resulting in a total of $8 \times 36 = 288$ simulations. While it might not be obvious that basic state variations from one winter to the next are small in the context of interannual variability such as El Niño–Southern Oscillation, our results below will demonstrate that this assumption is indeed valid and that certain MJO phases demonstrate teleconnection pattern consistency even in the presence of interannual basic state variability. Further, to ensure that the extratropical response is generated by the forcing within the typical duration of an MJO phase of 5 days (Henderson et al. 2017; lag 0–4), we gradually turn off the Q'_1 forcing by applying an e -folding factor of 5 days to the given forcing. It is worth mentioning that MJO heating is given to the LBM for each phase separately, which indicates that no MJO phase precedes the next MJO phase, although the MJO forcing for the particular phase still evolves throughout that phase. This may result in some differences between the LBM simulations and reanalysis data, and these differences will be discussed in the next section. However, this is not believed to be a bad assumption since MJO events across all phases on average maintain amplitude greater than 1 sigma for less than 10 days (Henderson et al. 2017).

For the FixBS experiment, we fix the basic state to the 1979–2015 boreal winter average and give the model MJO forcing from first 24 MJO events for each phase, which satisfies the criteria given above, resulting in a total of $8 \times 24 = 196$ simulations. An MJO event is defined based on the amplitude and duration criteria given above. We also apply the same e -folding factor to the heating in the FixBS experiment to make the experiment setup consistent.

b. Observational reference

1) 500-hPa GEOPOTENTIAL HEIGHT ANOMALIES

Typically, tropical–extratropical teleconnections have a barotropic structure away from the tropics; thus, we use the 500-hPa geopotential height as the major diagnostic variable, noting that other tropospheric layers give us similar results. In this study, to enable a comparison with Tseng et al. (2018), which used the Modern-Era Retrospective Analysis for Research and Applications (MERRA) for analysis, we employ ERA-Interim from 1979 to 2015 as the observational reference. The data are interpolated to a horizontal resolution of $2.5^\circ \times 2.5^\circ$. To remove the annual cycle, the 500-hPa geopotential height data are preprocessed with a similar approach to that applied to Q_1 . The only preprocessing difference between Z500 and Q_1 is that we do not apply the

intraseasonal band-passed filter to Z500, which enables a direct comparison with Tseng et al. (2018).

2) MJO INDICES

To create a proxy for MJO convection evolution, the OLR-based MJO index is used (Kiladis et al. 2014), which was acquired from <https://www.esrl.noaa.gov/psd/mjo/mjoindex/>. One advantage of using the OMI to define intraseasonal convective heating is that the OMI is purely based on outgoing longwave radiation, which is a good proxy for tropical deep convection. Planetary-scale convection (zonal wavenumbers 1–3) in the tropics has been proven to play a vital role in generating tropical–extratropical teleconnections in previous studies (Hoskins and Karoly 1981; Hsu 1996). Thus, the OMI is a more ideal MJO index for the purposes of this study than other indices defined by multiple variables.

c. Method

1) QUANTIFYING THE PATTERN CONSISTENCY

The approach of paired pattern correlations is used to quantify the pattern consistency of the teleconnections over different MJO events, a method that was documented in Tseng et al. (2018). For each phase and lag, one area-weighted anomalous pattern correlation coefficient of Z500 is derived from every two MJO events in the North Pacific (20°–70°N, 150°E–120°W). By calculating the fraction of pairs that meet or exceed a correlation coefficient of 0.5, we can estimate the pattern consistency for specific MJO phases and lags. The pattern correlation of anomalous fields has been widely used in operational centers as a metric to quantify prediction skill and Tseng et al. (2018) demonstrated that the MJO phases with consistent patterns of geopotential height anomalies are also characterized by improved model prediction skill. The mechanism that causes this MJO-phase dependent pattern consistency is a major focus of this study.

In Tseng et al. (2018), the pattern consistency was assessed in MERRA (their Fig. 3). To examine whether this analysis approach also works in ERA-Interim, we applied it to Z500 of ERA-Interim from the same 1979 to 2015 period (Fig. 1). The dark colors indicate higher pattern consistency of tropical–extratropical teleconnections over different MJO events while the bright colors represent lower pattern consistency. The dotted regions denote that the pattern consistency exceeds the 99% confidence bounds by a bootstrapping analysis. (For the bootstrapping analysis, we randomly resampled the data 500 times based on the sample size of each MJO phase and time lag to approximate the distribution of the fraction of pairs with high pattern correlations due to chance alone.)

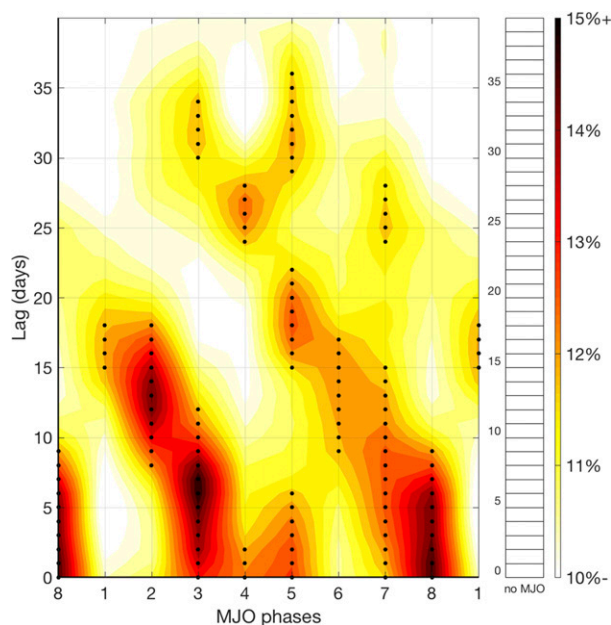


FIG. 1. The pattern agreement of Z500 (20°–70°N, 150°E–120°W) over different MJO events as quantified by pattern correlations. Shading indicates the occurrence frequency of any two events with correlation coefficient > 0.5. Dotted regions indicate the value is greater than the 99% confidence bounds based on a bootstrapping analysis. This is a recreation of Fig. 3 in Tseng et al. (2018) but now using ERA-Interim.

Looking at Fig. 1, we see two stair-like patterns of high pattern consistency that are nearly quantitatively identical to the result of Tseng et al. (2018) where the MERRA reanalysis was used. This indicates that the approach used in Tseng et al. (2018) is also reproducible using other reanalysis data. In the following section, we apply the same analysis approach to the LBM simulations and test whether the LBM can reproduce these results.

2) LINEARIZED ROSSBY WAVE SOURCE

To investigate the Rossby wave source that triggers teleconnected patterns in the extratropical regions, we use the linearized barotropic vorticity equation (Sardeshmukh and Hoskins 1988; Seo and Lee 2017), applied to both the LBM simulations and ERA-Interim:

$$\frac{\partial \zeta'}{\partial t} = S' - \bar{\mathbf{V}}_{\psi} \cdot \nabla \zeta' - \mathbf{V}'_{\psi} \cdot \nabla \bar{\zeta} + F'. \quad (2)$$

In (2), the terms with primes indicate intraseasonal time scale anomalies and overbars denote the basic state. Here ζ is the absolute vorticity, \mathbf{V}_{ψ} is the rotational wind, S is the Rossby wave source, and F is the frictional term. The linearized Rossby wave source is contributed by four different terms:

$$S' = -\bar{\zeta}\nabla \cdot \mathbf{V}'_{\chi} - \mathbf{V}'_{\chi} \cdot \nabla \bar{\zeta} - \zeta' \nabla \cdot \bar{\mathbf{V}}_{\chi} - \bar{\mathbf{V}}_{\chi} \cdot \nabla \zeta'. \quad (3)$$

In general, the vorticity tendency in (2) is dominated by the rotational flow-induced advection (the second and third terms on the right side). However, in regions of active deep convection, the Rossby wave source term can be large and influence wave generation. In (3), the first two terms on the right side indicate the stretching of climatological absolute vorticity by the divergence of the anomalous flow ($-\bar{\zeta}\nabla \cdot \mathbf{V}'_{\chi}$) and the advection of climatological absolute vorticity by the anomalous divergent flow ($-\mathbf{V}'_{\chi} \cdot \nabla \bar{\zeta}$). The last two terms are the stretching of anomalous vorticity by the climatological divergence ($-\zeta' \nabla \cdot \bar{\mathbf{V}}_{\chi}$) and the advection of anomalous vorticity by the climatological divergent flow ($-\bar{\mathbf{V}}_{\chi} \cdot \nabla \zeta'$). In Mori and Watanabe (2008) and Seo and Lee (2017), the authors noted that the first two terms on the right side of (3) are the dominant terms on intraseasonal time scales. By calculating the Rossby wave source [S' in (3)], we can relate the Rossby wave source pattern in the subtropical and extratropical regions to the teleconnection pattern consistency that varies as a function of MJO phase and lag.

3. Teleconnections in LBM

In this section, we address the following questions. 1) Can the LBM simulate the phase-dependent pattern consistency that is found in reanalysis data? 2) How does the pattern consistency of MJO-induced teleconnections respond to modest variations in the basic state and MJO heating?

a. Model forcing and basic states

Figure 2 shows the MJO phase composite of column-integrated Q'_1 (shading) used in the FixQ1 experiment. The composited patterns show that MJO-related convection initiates in the central Indian Ocean in phases 1 and 2, strengthens in the eastern Indian Ocean, and then dissipates around the date line in phases 7 and 8. The average duration of each phase is ~ 5 days, which is consistent with previous studies (Henderson et al. 2017) and provides motivation for our experimental design. For the FixQ1 experiment, we use the composite Q'_1 indicated by the shading in Fig. 2. The contours in Fig. 2 show the standard deviation of the column-integrated Q'_1 over different MJO events used in the FixBS experiment. In general, the contours are collocated with regions of maximum Q'_1 , although some regions and phases exhibit less good agreement. For example, the farther eastward extent of contours compared to the shading in the central Pacific likely results from interannual variability of MJO heating associated with ENSO (Hendon et al. 1999).

Basic state winds and their variability are shown in Fig. 3. The shading represents the boreal winter zonal wind at 200 hPa averaged from 1979 to 2015, and the contours are the standard deviation of the zonal wind over the 36 boreal winter means for different years used in the FixQ1 experiment. Generally, two dominant features are apparent: the North Pacific jet stream and the North Atlantic jet stream, which are found to the east of Asia and North America, respectively, between 30° and 40°N . The contours in Fig. 3 show the interannual variability of the jet streams, including the eastward extension and northward or southward shift of the jets. The jet shifts likely result from interannual variability associated with ENSO. Typically, the subtropical jet extends eastward and equatorward during El Niño years, and westward and poleward in La Niña years. The combination of information from the shading in Fig. 2 and the contours in Fig. 3 can be used to test how MJO-induced teleconnections evolve with modest variations of the jet stream and other aspects of the basic state (i.e., our FixQ1 experiment). Similarly, if we exploit information from the contours in Fig. 2 (i.e., the MJO heating variability over different events) and the shading in Fig. 3 (i.e., the climatological basic state), we can test the sensitivity of the teleconnected responses to modest variations of tropical heating, which comprise the FixBS experiment. In reality, both the basic state and MJO heating change together (e.g., during ENSO warm events), however, this kind of linearized experimental design can help us simplify the questions and access the key mechanisms in a more tractable manner.

b. Z500 composites

The shading in Figs. 4 and 5 represents the MJO phase- and lag- composited Z500 in FixQ1 and FixBS, respectively. The contours in Figs. 4 and 5 show the same field from ERA-Interim. In Fig. 4, both observations and the LBM simulations indicate positive Z500 in the North Pacific during MJO phases 2 and 3, while the opposite patterns can be found in phases 6 and 7 associated with opposite-signed MJO heating in the tropics. This PNA-like pattern has been widely documented in observational studies and numerical simulations (Mori and Watanabe 2008; Seo and Lee 2017). Although the observed teleconnection pattern is generally collocated with the simulated pattern, some inconsistency still exists. For example, the amplitude of the simulated teleconnections is systematically smaller than the observed teleconnections in Fig. 4. Held et al. (1988) noted that a linear model might underestimate the amplitude of tropical–extratropical teleconnections due to the lack of dynamical feedbacks from transient eddies. Hirota and Takahashi (2012) also pointed out the lack of diabatic

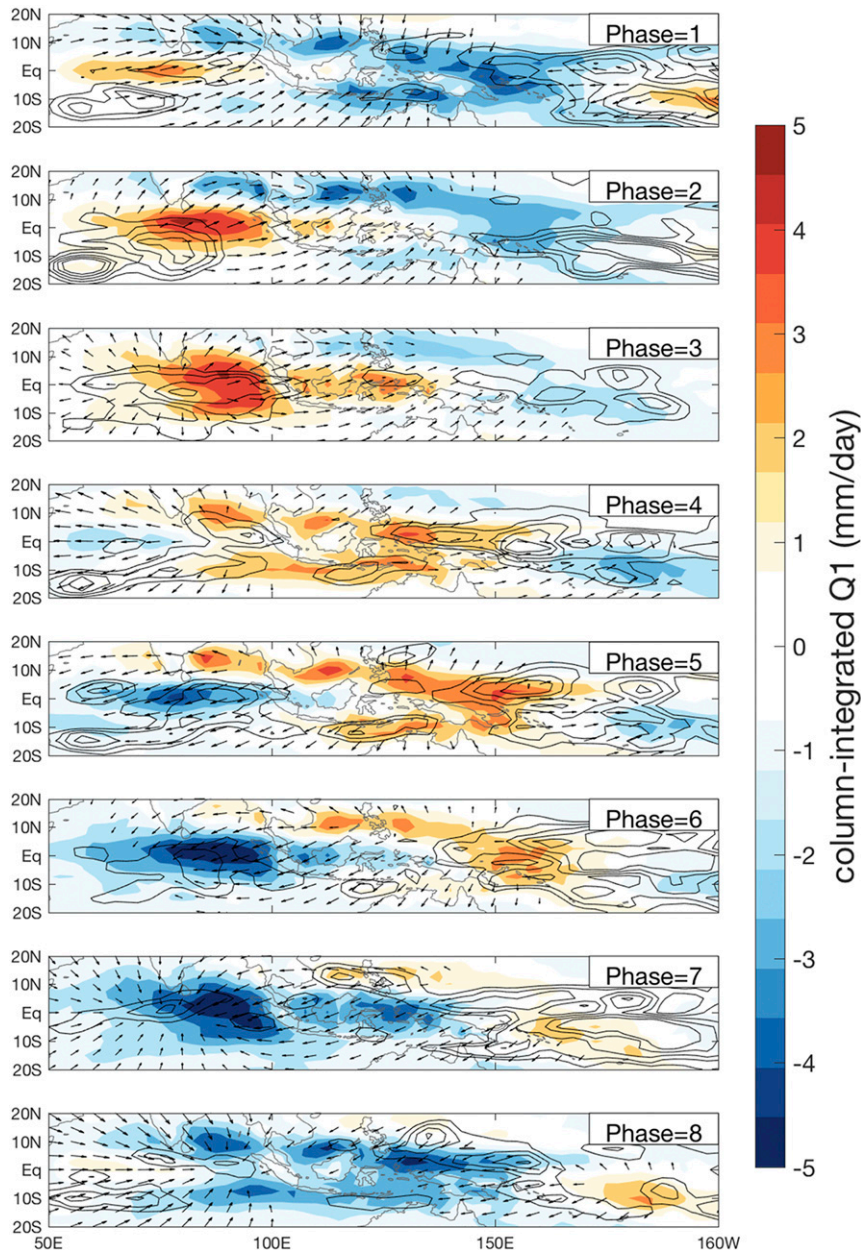


FIG. 2. The MJO phase composited column-integrated Q_1 used in the FixQ1 experiment (shading; mm day^{-1}) and the standard deviation of the intraseasonal time scale column-integrated Q_1 over the different events used in FixBS (contours, from 3 to 5 mm day^{-1} with interval of 0.5 mm day^{-1}). The vector shows the MJO phase composited 200-hPa divergent wind; vectors with amplitude smaller than 0.8 m s^{-1} are omitted.

heating feedbacks can lead to an underestimation of teleconnection amplitude. In addition, the nonlinear feedback from zonal mean–eddy interactions that might amplify the teleconnections is also absent in the model (Kimoto et al. 2001; Watanabe and Jin 2004). Looking more closely at Fig. 4, we also see that the strongest observed teleconnections are found diagonally (see

contours; e.g., similar spatial structure and strength patterns shows up in MJO phase 1, lag 15–19; MJO phase 2, lag 10–14; and MJO phase 3, lag 5–9) while the strongest simulated teleconnections are more concentrated in specific MJO phases. Since the MJO propagates in the real world, where one phase is often followed by the next phase and each phase typically lasts

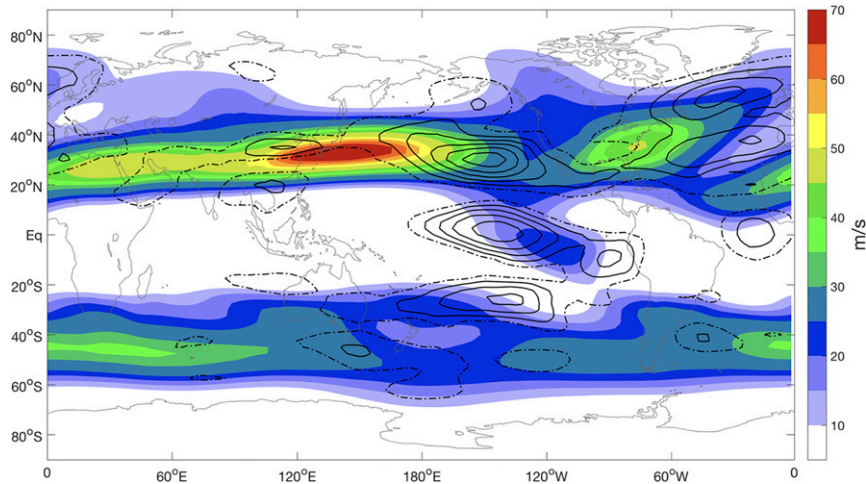


FIG. 3. The 200-hPa climatological zonal wind in DJF (shading; m s^{-1}) and the standard deviation of DJF-averaged zonal wind over different years from 1979 to 2015. Contours start at 5 m s^{-1} with an interval of 1 m s^{-1} . The dashed contour denotes the isoline of 5 m s^{-1} .

for 5 days, the composited signal is stronger diagonally across phase-lag space in observations than the LBM, where MJO heating is given to the model separately in different phases for both FixQ1 and FixBS. Overall, however, the LBM can reasonably reproduce the MJO-induced teleconnections observed in the reanalysis data, although with some differences caused by the experimental design and the model dynamics.

Comparing the teleconnected patterns between two experiments, the shading in Figs. 4 and 5 generally indicates similar behavior. Both experiments show stronger composited amplitudes in specific MJO phases, such as phases 2, 3, 6, and 7. This suggests two possibilities: 1) the signal is dominated by a few strong simulations in these phases or 2) a similar teleconnection pattern occurs more frequently in these phases compared to others. We provide a more detailed discussion of these possibilities in the next subsection. One notable difference between Figs. 4 and 5 is that the amplitude of composited $Z500$ is higher in FixBS. Since we conducted these two experiments in a linearized model with identical setups except for the initial conditions, the amplitude of response is directly proportional to the amplitude of given forcing, especially with the perturbed heating locations occurring in the same general vicinity among events. On average, the amplitude of composited Q_1' in FixQ1 is 40% smaller than the amplitude of individual events in FixBS. Thus, the teleconnected response largely reflects the amplitude difference of the given forcing. One might think that the FixBS and FixQ1 experiments should lead to the same composite amplitude of $Z500$ since the model used here is linear. However, this would only be true only if the basic states were identical in FixQ1 and

FixBS. Since the basic states are different between these two experiments, FixBS and FixQ1 show different composite amplitudes.

c. Pattern consistency in LBM

Since a large composite amplitude could result from only a few dominant MJO events while most of other events are weak, Figs. 4 and 5 provide limited information about the occurrence frequency of the teleconnection patterns or the pattern consistency over different events. Here, we calculate the pattern correlation of $Z500$ in the region of $20^\circ\text{--}70^\circ\text{N}$, $150^\circ\text{E}\text{--}120^\circ\text{W}$ to quantify the similarity over different model realizations in FixQ1 and FixBS. Figure 6a is the equivalent plot of Fig. 1, but for the FixQ1 experiment. The dark colors in Fig. 6 indicate that more simulation pairs have similar teleconnection patterns and the light colors indicate that fewer simulation pairs have similar teleconnection patterns. In Fig. 6a for FixQ1, high pattern consistency appears right after model initialization and decays with time. Since forcing is identical from one simulation to the next in FixQ1, the tropical response directly induced by the heating should be similar (e.g., resembling the Gill pattern; Gill 1980). With increased model lead time, the MJO heating starts to interact with the different basic states. Thus, the pattern consistency dramatically decreases around day 5 for most MJO phases, which is also the e -folding time used to decay the heating. However, some phases show prolonged periods of high pattern consistency (e.g., phases 2, 3, 6, and 7) and these are also the phases showing large amplitudes of composited $Z500$ in Fig. 4. After day 30, all MJO phases show relatively low pattern consistency. The trend of decreased pattern consistency over all MJO

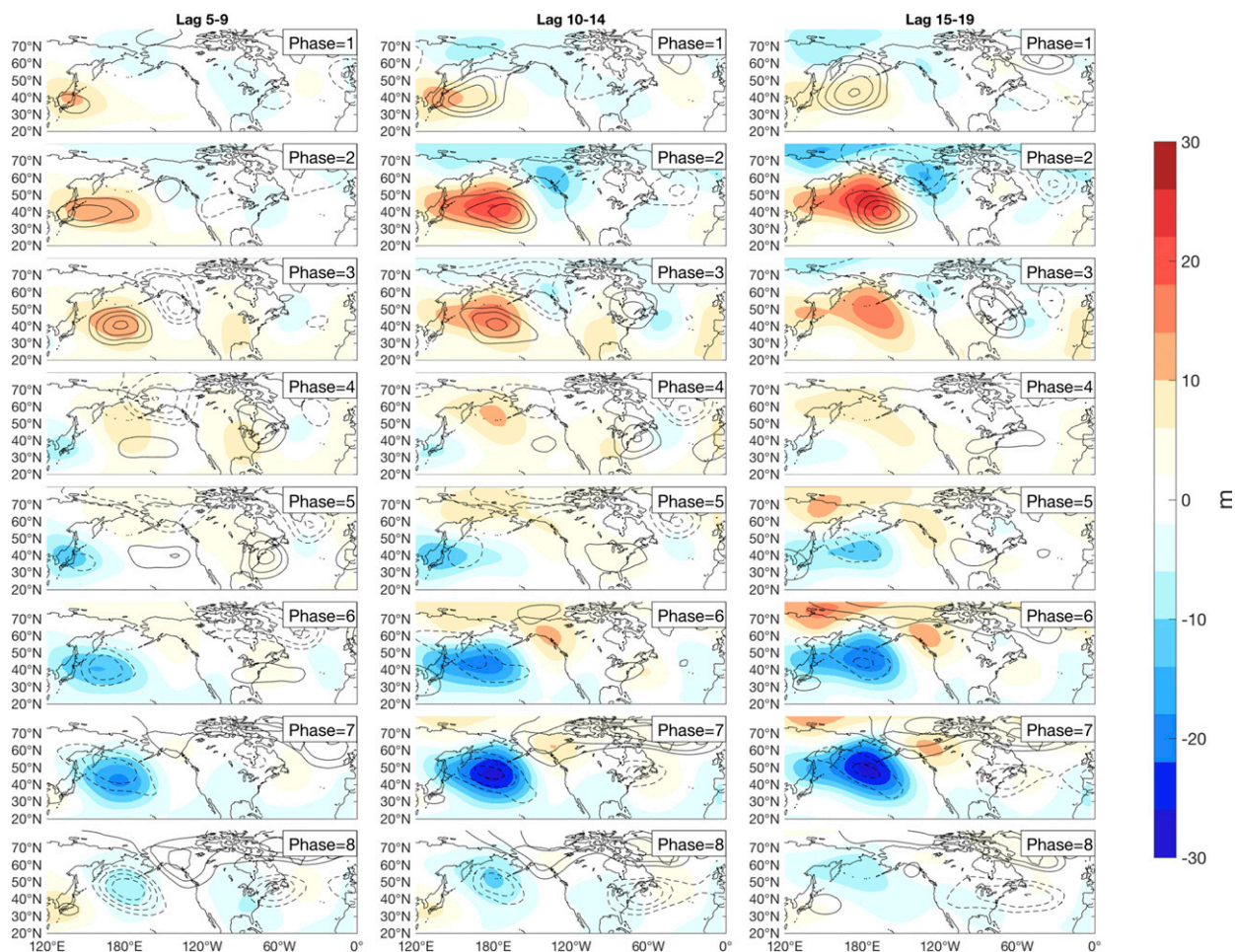


FIG. 4. MJO phase- and lag-composites of Z500 in the FixQ1 experiment (m; shading) and ERA-Interim (m; contour). Solid contours denote positive anomalies and dashed contours denote negative anomalies. The contour interval is 10 m starting at ± 20 m.

phases likely results from the different basic states, which determine the ultimate patterns of Z500. One concern is whether the domain selection can influence the results in Fig. 6a. To test this, we conducted a series of sensitivity tests by moving the southern boundary northward every 5° of latitude (not shown). With this shifting of the southern boundary, the high pattern consistency in the early lags decreases, verifying the hypothesis that the high pattern consistency in early lags results from the tropical response directly induced by the heating.

For the FixBS experiment (Fig. 6b), the percentages of pairs with high pattern consistency is low in the first 10 days and then increases for phases 2, 3, 6, 7, and 8 after day 10. The timing of the high pattern consistency in Fig. 6b corresponds well to the timing of large composite amplitude in Fig. 5. As we mentioned previously, the Gill-like response is driven by the given heating immediately after model's initialization. The highly diverse Z500 patterns before day 10 could result from different forcings and hence different direct circulation responses at short lead

times. One might argue that 500 hPa is a region of near nondivergence in the tropics and hence subtle changes in the height of nondivergence from one MJO event to the next could produce different signed geopotential height anomalies over different events, making it unlikely to achieve high pattern consistency at small leads. Thus, we conducted another sensitivity test that examined the pattern consistency of the 200-hPa geopotential height anomalies rather than those at 500 hPa (figure not shown). The calculation based on 200-hPa geopotential height is nearly identical to the calculation based on 500-hPa geopotential height. Thus, the result is not sensitive to the choice of vertical layer. Regardless, even though a variety of heating patterns are given in FixBS, high pattern consistency still appears around day 10 for specific MJO phases, and these are also the phases that show prolonged periods of high pattern consistency in FixQ1. The time lag of 10 days likely arises from the weakening influence of the direct Gill-like responses that vary from event to event associated with different heating anomaly structures, and

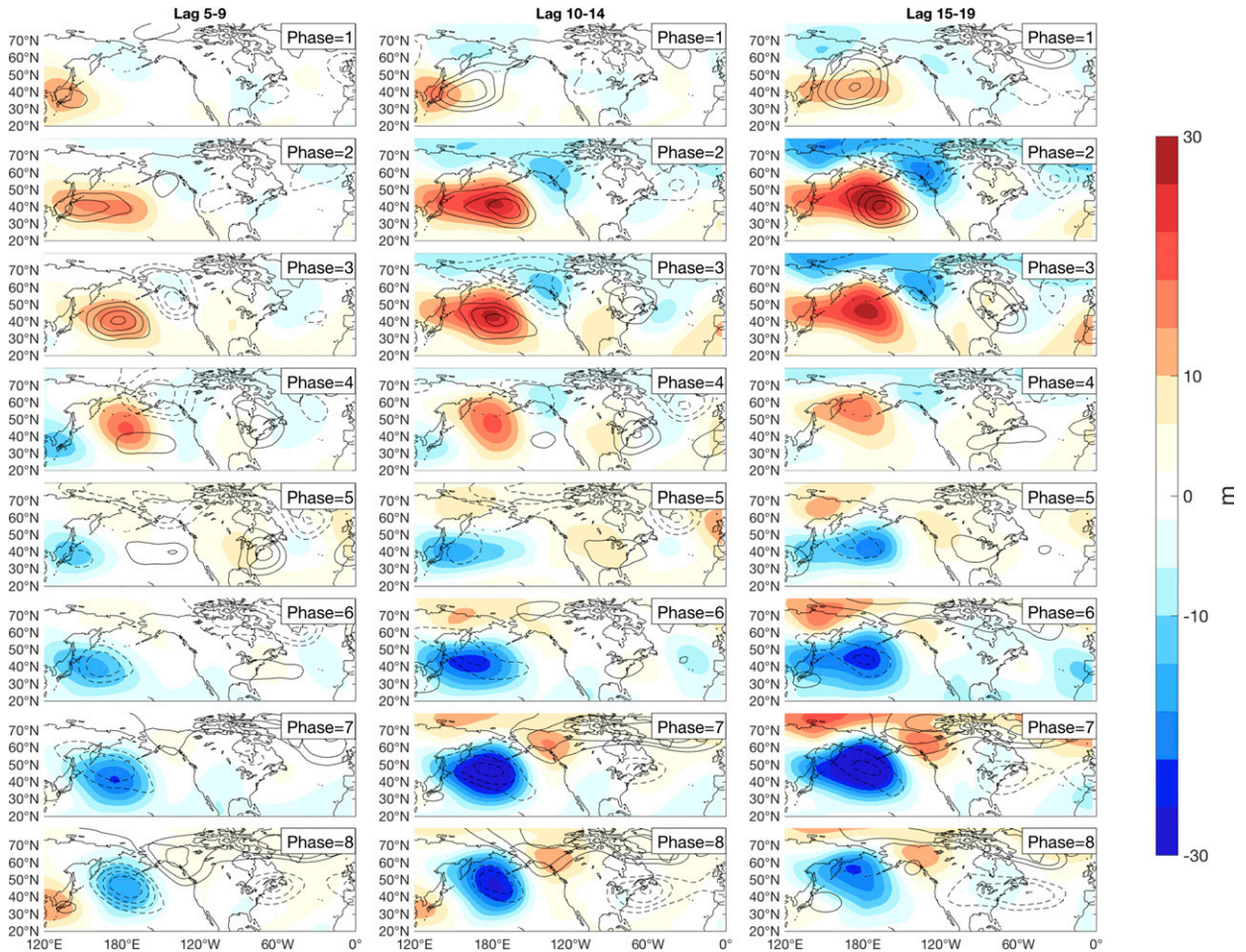


FIG. 5. MJO phase- and lag-composites of Z500 in the FixBS experiment (m; shading) and ERA-Interim (m; contour). Solid contours denote positive anomalies and dashed contours denote negative anomalies. The contour interval is 10 m starting at ± 20 m.

the time it takes to establish the tropical–extratropical teleconnection determined by the basic state and Rossby wave propagation. Note that the phases with higher pattern consistency in FixBS show a longer period of greater consistency (up to day 35) compared to FixQ1, and this is likely caused by the identical basic states in FixBS. Generally, Figs. 6a and 6b indicate that regardless of modest variations in the basic states and heating patterns, the teleconnection patterns during MJO phases 2, 3, 6, and 7 are very consistent from one realization to the next, suggesting that the geographical location of the heating anomalies (i.e., MJO phase) is responsible for such consistency. This will be explored further in the next section.

4. Rossby wave source analysis

a. Rossby wave source consistency as a function of MJO phase in the LBM

To assess the key mechanisms for why heating in specific MJO phases and geographical locations favors

consistent teleconnection patterns while others do not, we employ the linearized Rossby wave source based on (3). The dots in Fig. 7 show the sign agreement of the linearized Rossby wave source at 200 hPa [S' in (3)] at lag 1 for different MJO phases in FixQ1. Dotted regions indicate that over 70% of the realizations (i.e., more than 25 realizations) agree on a positive sign or negative sign of the linearized Rossby wave source. (Note that since FixBS has similar patterns, we only show the results from FixQ1 here.) In general, Fig. 7 indicates two interesting features: 1) The regions with high agreement of the Rossby wave source over all MJO phases are all concentrated near the East Asia jet (25° – 40° N, 110° E– 180°), and 2) the sign agreement of the linearized Rossby wave source evolves with MJO phase, showing either a symmetric or an asymmetric pattern about 135° E. The latter point can be explained by examining the terms in (3). Two terms in (3) are associated with energy conversions from the basic state vorticity to the anomalies. The first term, $-\bar{\zeta} \nabla \cdot \mathbf{V}'_{\chi}$, is proportional to the amplitude of the

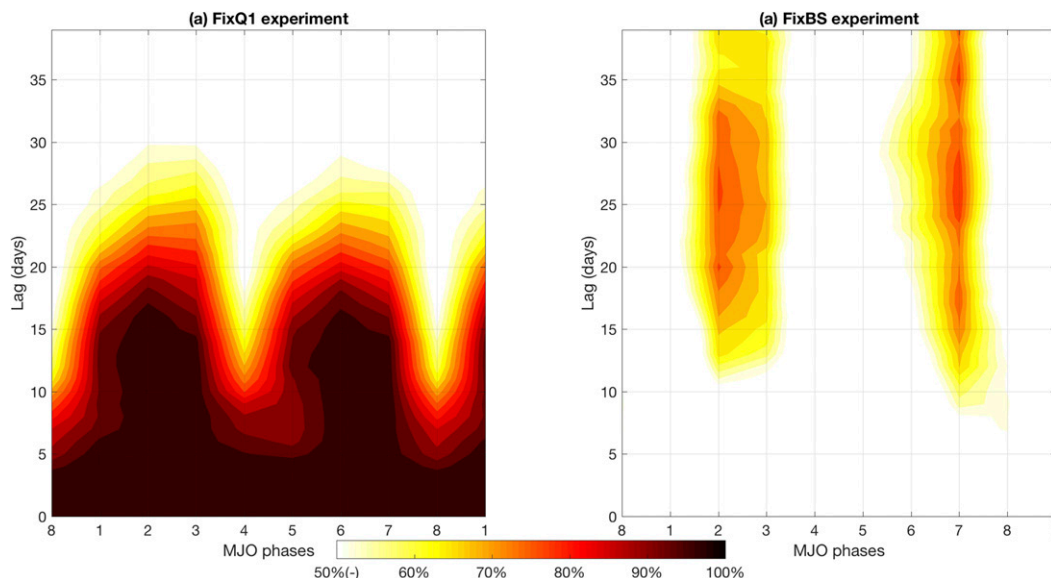


FIG. 6. The pattern agreement of Z500 (20° – 70° N, 150° E– 120° W) over different MJO simulations as quantified by pattern correlations in (a) the FixQ1 experiment and (b) the FixBS experiment. Shading indicates the occurrence frequency of any two simulations with correlation coefficient >0.5 . A value of 100% indicates that all simulation pairs have pattern correlations that exceed 0.5.

climatological vorticity and the second term, $-\mathbf{V}'_{\chi} \cdot \nabla \bar{\zeta}$, is proportional to the gradient of the climatological vorticity. Typically, the jet regions are characterized by the strongest zonal and meridional wind gradients, thus providing favorable conditions for producing vorticity anomalies and a strong Rossby wave source. As for the symmetry of the Rossby wave source about 135° E, because the direction of the anomalous upper-tropospheric divergent wind evolves with MJO phase (vectors in Fig. 2), the sign of the linearized Rossby wave source is also affected. For example, when the convective signal is located in the eastern Indian Ocean (e.g., MJO phases 2 and 3), the intraseasonal divergent flow at 200 hPa is southwesterly in the eastern Indian Ocean and the Indochina peninsula and northwesterly in the northwestern Pacific. This kind of divergent flow pattern can result in a negative Rossby wave source to the west of 135° E (the dashed line in Fig. 7) and a positive Rossby wave source to the east of 135° E (see also Seo and Lee 2017). In contrast to the MJO heating in the eastern Indian Ocean, anomalous convection in the western Pacific can generate a nearly identical Rossby wave source pattern with opposite sign near the jet regions. In addition, the divergence of the intraseasonal flow (i.e., $\nabla \cdot \mathbf{V}'_{\chi}$) also evolves with MJO phase. When the MJO convection is located in the eastern Indian Ocean, the jet exit region is characterized by the anomalous upper-tropospheric convergence and the jet entrance region is characterized by anomalous divergence. When MJO convection is located in the western Pacific, the jet exit region is

characterized by anomalous upper-tropospheric divergence and the jet entrance region is characterized by anomalous convergence. In general, $-\bar{\zeta} \nabla \cdot \mathbf{V}'_{\chi}$ and $-\mathbf{V}'_{\chi} \cdot \nabla \bar{\zeta}$ add constructively to each other over the eight MJO phases. The other terms in the Rossby wave source are small, consistent with previous studies (e.g., Seo and Lee 2017).

b. The role of tropical heating

Further inspection of Fig. 7 shows that the phases with more dipole-like patterns of sign agreement of the Rossby wave source are also the phases characterized by higher pattern consistency on S2S time scales (e.g., phases 2, 3, 6, and 7). In addition, these are also the MJO phases showing a dipole heating structure across the eastern Indian Ocean and the western Pacific (Fig. 2). Thus, we conduct two experiments to clarify the roles of heating in the eastern Indian Ocean and the heating in the western Pacific for generating the dipole-like Rossby wave source and associated tropical–extratropical teleconnection pattern. The first simulation contains positive-only heating from the MJO phase 2 composite (Fig. 8a) and a fixed climatological basic state. The second simulation has an identical setup to the first simulation except that MJO phase 6 positive-only heating is used (Fig. 8b). We examine the extratropical response 10 days after we prescribe the forcings. Results of the simulations are shown in Figs. 8c–f. Figure 8c and 8d are the Rossby wave source patterns generated by MJO heating in MJO phase 2 and phase 6 simulations,

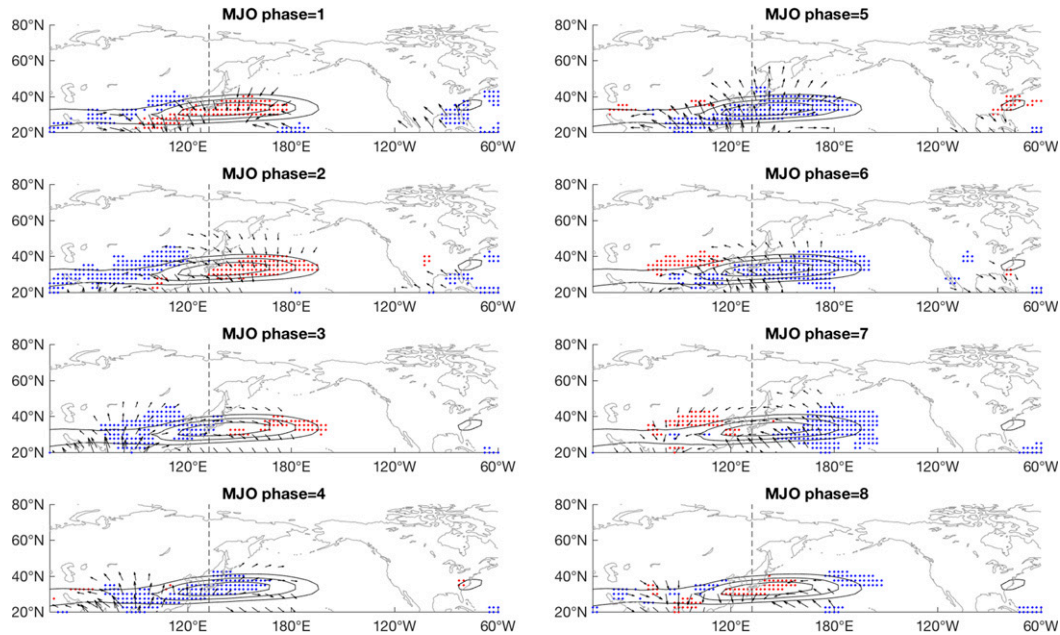


FIG. 7. The sign agreement of the 200-hPa anomalous Rossby wave source at a lag of 1 day over different simulations of the FixQ1 simulations. Red dots indicate positive Rossby wave source anomalies with occurrence frequency $>70\%$ and blue dots indicate negative Rossby wave source anomalies with occurrence frequency $>70\%$. Dashed vertical lines demarcate 135°E and the contours denote the 200-hPa climatological zonal wind at 45, 55, and 65 m s^{-1} . The vector shows the MJO-phase composited 200-hPa divergent wind in LBM at a lag 1 day; vectors with amplitude smaller than 0.8 m s^{-1} are omitted.

respectively. Figures 8c and 8d indicate that heating both in the eastern Indian Ocean and the western Pacific can generate an asymmetric structure of the Rossby wave source around the jet. The slightly stronger Rossby wave source in the jet entrance region for MJO phase 2, and the jet exit region for MJO phase 6, likely results from the proximity of the forcing center. The corresponding teleconnection patterns for the two simulations are shown in Figs. 8e and 8f. Because of the opposite Rossby wave source pattern around the jet regions, Figs. 8e and 8f show similar PNA-like patterns, but with opposite sign. Because of the linearity of the LBM, the sign of the heating either in the eastern Indian Ocean or the western Pacific can simply be flipped to show that the MJO phases characterized by dipole heating (i.e., phases 2, 3, 6, and 7) are more likely to have strong teleconnection signals because of the constructive superimposition of similar teleconnected patterns. The enhanced signal could lead the MJO-induced teleconnections to emerge from the background variability in the observations and increase the pattern consistency. This result is consistent with Seo and Lee (2017), who showed that anomalous heating in both the eastern Indian Ocean and the western Pacific has comparable roles in generating PNA-like teleconnection patterns in the extratropical Pacific. With that said, the simulations

above do not directly explain why the MJO phases characterized by a symmetric Rossby wave source have lower pattern consistency. This will be addressed further in the next section, especially when considering Rossby wave sources that are symmetric about 135°E .

5. Dynamics of consistent teleconnections in the reanalysis

In section 4, we demonstrated that the MJO phases with a more asymmetric pattern of the Rossby wave source are also the phases with more consistent teleconnection patterns in the LBM. Our subsequent heating location tests showed that MJO convection in the eastern Indian Ocean and the western Pacific can generate similar PNA-like patterns, but with opposite sign because of the opposite Rossby wave source generated about the jet. This provides some clue as to why specific MJO phases favor a more consistent tropical–extratropical teleconnection pattern. However, section 4 only demonstrated that a single convectively driven forcing, either in the eastern Indian Ocean or the western Pacific, can generate a dipole structure of Rossby wave source in the LBM across the jet. This does not yet answer, however, why the MJO phases characterized by a symmetric Rossby wave source have less consistent teleconnections. Further, all of

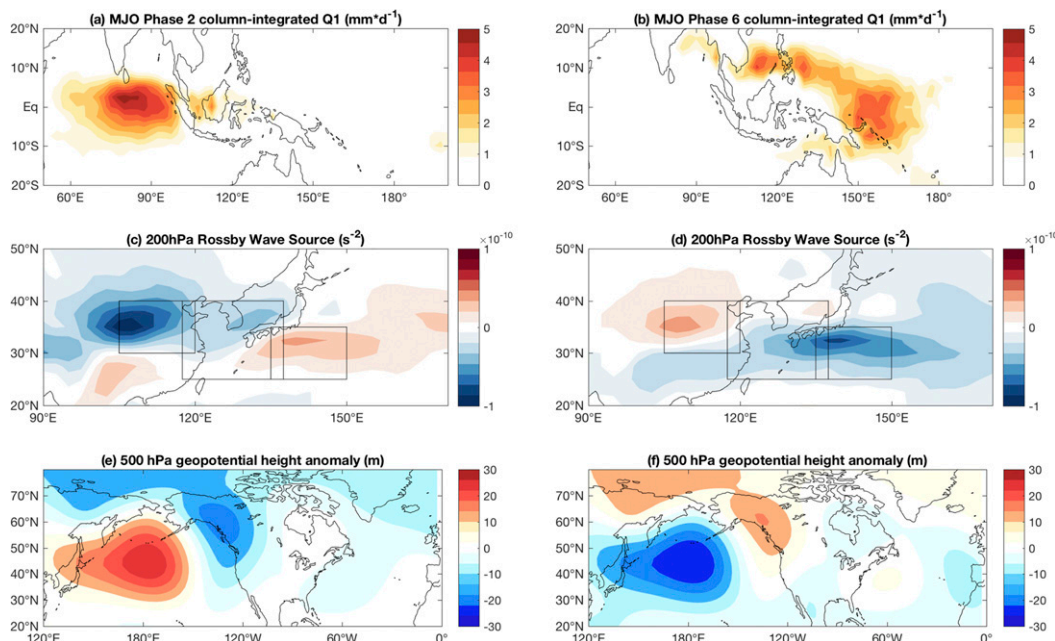


FIG. 8. LBM simulations with positive-only heating and the climatological basic state. (a) MJO phase 2 column-integrated Q_1 (mm day^{-1}); (b) MJO phase 6 column-integrated Q_1 (mm day^{-1}); (c) the 200-hPa Rossby wave source generated by heating in (a); (d) the 200-hPa Rossby wave source generated by heating in (b); (e) the simulated 500-hPa geopotential height anomaly at lag 10 with heating in (a); (f) the simulated 500-hPa geopotential height anomaly at lag 10 with heating in (b).

these tests are based on an LBM. The real world might act in a more complicated manner than a linear system. Thus, in this section, we present a statistical view to examine the relationship between the Rossby wave source around the jet and the pattern consistency of teleconnections in ERA-Interim.

a. Composite patterns of Z500 based on the Rossby wave source

To demonstrate how the Rossby wave source across the subtropical jet influences the variability of tropical–extratropical teleconnections in the reanalysis data, we use the standardized time series of the area-averaged Rossby wave source at lag 1 in two reference regions. The first region is located at 30°–40°N, 105°–120°E (EI_{RWS} ; the left box shown in Figs. 8c,d) and the other is located at 25°–35°N, 135°–150°E (WP_{RWS} ; the right box shown in Figs. 8c,d). These two regions are also the regions showing the strongest Rossby wave source signals in Figs. 8c and 8d. The indices are named based on which heating center (eastern Indian Ocean heating or western Pacific heating) is the more dominant contributor to the Rossby wave source. Figure 9 depicts the composited Z500 at lag 10 over the extratropical Pacific for different combinations of EI_{RWS} and WP_{RWS} . From Figs. 9c–f, it is found that either strong EI_{RWS} or strong

WP_{RWS} can generate PNA-like composite patterns in the extratropical Pacific. For example, when EI_{RWS} is greater than one standard deviation and the amplitude of WP_{RWS} is less than one standard deviation (Fig. 9d), the composited Z500 shows a positive PNA-like pattern with a low pressure anomaly in the North Pacific and high pressure anomaly in Alaska. A nearly opposite pattern of composited Z500 can be found when EI_{RWS} is smaller than minus one standard deviation and the amplitude of WP_{RWS} is smaller than one standard deviation (Fig. 9c). Figures 9e and 9f show that WP_{RWS} generates similar teleconnection patterns to EI_{RWS} , except with an opposite sign. In general, the information from Figs. 9c–f suggests that a dipole structure of the Rossby wave source around the jet regions is likely to give rise to an enhanced teleconnection signal while a symmetric Rossby wave source can reduce the teleconnection signal. To verify this point, Figs. 9a, 9b, 9g, and 9h show four scenarios, including the dipole structure of the Rossby wave source and the symmetric structure of the Rossby wave source across the subtropical jet. In Figs. 9a and 9b, the composited Z500 shows a similar PNA-like pattern to the composited pattern in Figs. 9e and 9f but the composited amplitudes are stronger for a dipole structure of the Rossby wave source. In Figs. 9g and 9h for a symmetric Rossby wave source with same

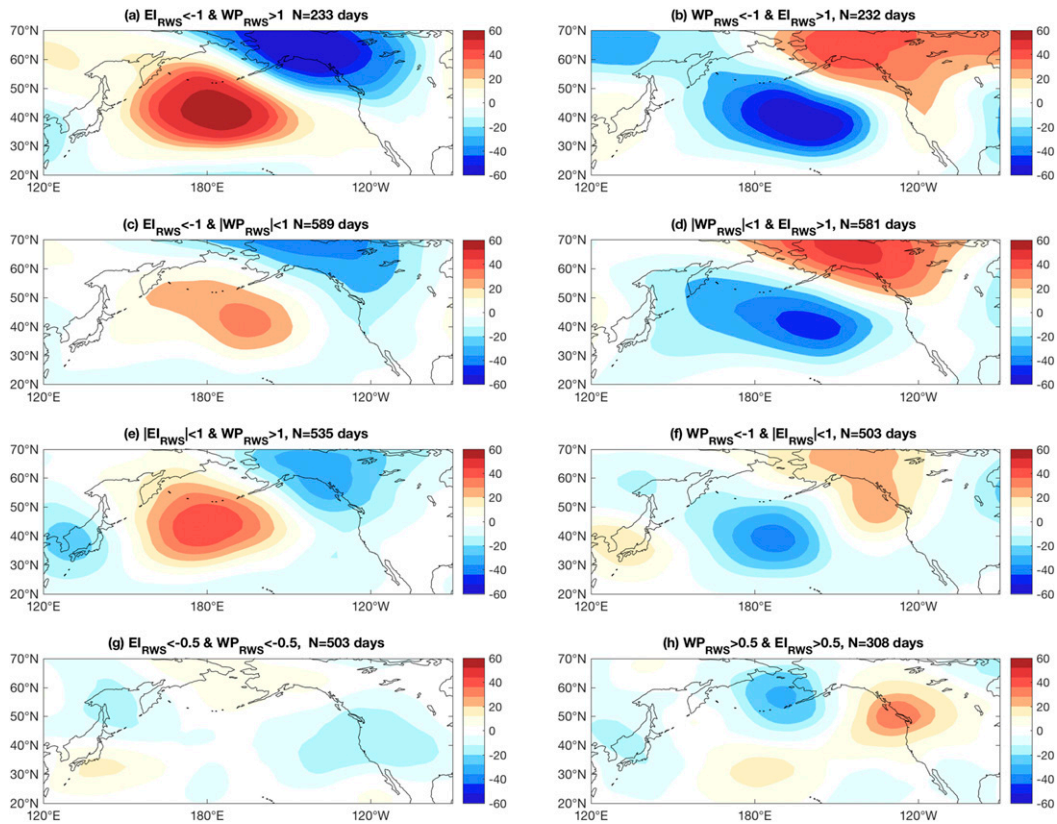


FIG. 9. The composited geopotential height anomaly at lag 10 from ERA-Interim for (a) $EI_{RWS} < -1\sigma$ and $WP_{RWS} > 1\sigma$, (b) $WP_{RWS} < -1\sigma$ and $EI_{RWS} > 1\sigma$, (c) $EI_{RWS} < -1\sigma$ and $|WP_{RWS}| < 1\sigma$, (d) $|WP_{RWS}| < 1\sigma$ and $EI_{RWS} > 1\sigma$, (e) $|EI_{RWS}| < 1\sigma$ and $WP_{RWS} > 1\sigma$, (f) $WP_{RWS} < -1\sigma$ and $|EI_{RWS}| < 1\sigma$, (g) $EI_{RWS} < -0.5\sigma$ and $WP_{RWS} < -0.5\sigma$, and (h) $EI_{RWS} > 0.5\sigma$ and $WP_{RWS} > 0.5\sigma$. EI_{RWS} is defined as the standardized time series of the domain-averaged Rossby wave source from 30° – 40° N and 105° – 120° E. WP_{RWS} is defined as the standardized time series of the domain-averaged Rossby wave source from 135° – 150° E and 25° – 35° N.

sign to either side of 135° E, the teleconnection pattern is qualitatively different and weaker. These results verify the importance of a dipole Rossby wave structure for producing a robust teleconnection.

Although Fig. 9 shows that a dipole Rossby wave source can favor a strong Z500 composite pattern, one might argue that the Rossby wave source index defined previously is not representative enough of all MJO phases. According to Fig. 7, the sign agreement of the Rossby wave source shows either a monopole or a tripole structure in MJO phases 1, 4, 5, and 8. Our earlier two domains filter out the monopole cases. Thus, we revisit the Z500 composite pattern to include the domain averaged value of the Rossby wave source in the region of 25° – 40° N, 117.5° – 147.5° E (MC_{RWS} ; i.e., the Maritime Continent region, the middle box shown in Figs. 8c and 8d). Figure 10 depicts the Z500 composite patterns at a lag of 10 days for different combinations of MC_{RWS} , EI_{RWS} , and WP_{RWS} . In Fig. 10, we see that the average amplitude of Z500 is weak (typically smaller

than 40 m) compared with Figs. 9a–d when MC_{RWS} is greater than 1σ or smaller than -1σ . Figure 10 implies that the extratropical response is likely to be less sensitive to variations of MC_{RWS} . However, the weak composite amplitude of Z500 can arise from strong, but highly varied, patterns over different events or weak amplitudes in individual events. Additional discussion of these issues is presented in section 5b.

b. Pattern consistency of Z500 according to a Rossby wave source–based index

In Fig. 9, the composite analysis showed that the distribution of the Rossby wave source across the subtropical jet can have a strong influence on the composited Z500 signals. Of interest is whether a similar influence is found for the pattern consistency of Z500. To examine this, in Fig. 11a we divide EI_{RWS} and WP_{RWS} into several bins of width 0.5σ . For each bin, the pattern consistency of Z500 at lag 10 is calculated based on the approach given in section 2. If the sample size is less than 30, the calculated

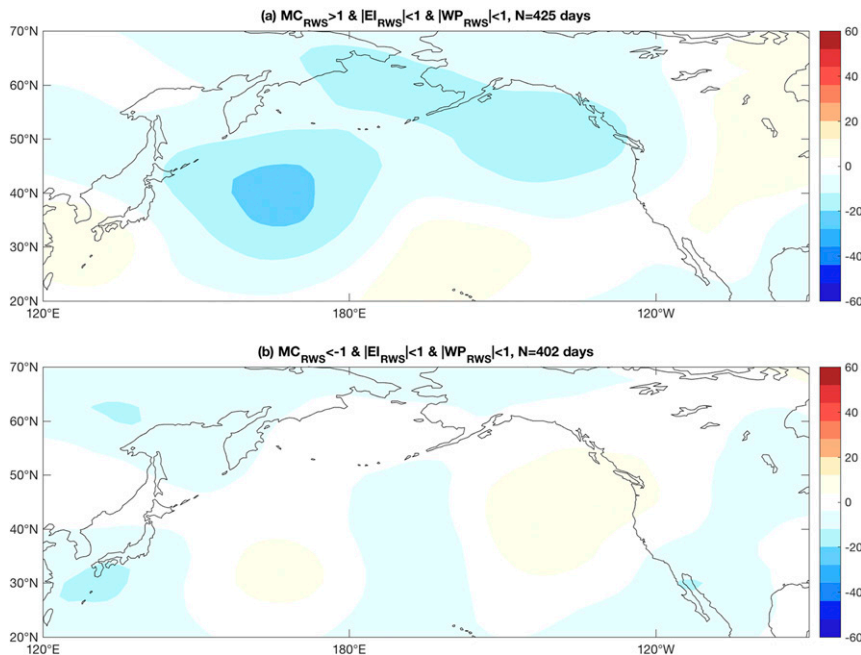


FIG. 10. The composited geopotential height anomaly (m) from ERA-Interim for (a) $MC_{RWS} > 1\sigma$, $|WP_{RWS}| < 1\sigma$, and $|EI_{RWS}| < 1\sigma$ and (b) $MC_{RWS} < -1\sigma$, $|WP_{RWS}| < 1\sigma$, and $|EI_{RWS}| < 1\sigma$. MC_{RWS} is defined as the standardized time series of the domain-averaged Rossby wave source from 25° – 40° N and 117° – 147.5° E.

value is omitted. The five different dot sizes range from small to large corresponding to different pattern consistencies ranging from 11%–19% with an interval of 2%. Values below 11% are omitted (the climatological value of pattern consistency is around 11%). Figure 11a shows that the regions with high pattern consistency are mostly concentrated in the second and the fourth quadrants. These are the quadrants that produce a dipole structure of the Rossby wave source. In addition, the small dots are mostly located in the first and the third quadrants, which are the quadrants having a symmetric structure of Rossby wave source. This result verifies the hypothesis in section 5a that the constructive superposition of the teleconnections produced by opposite-signed Indian Ocean and west Pacific heating not only enhances the composite amplitude but also increases the pattern consistency of Z500. It further suggests that the destructive interference of teleconnections by the Rossby wave source on each side of the jet can diminish the amplitude of composited Z500 and decrease the pattern consistency in the case of a symmetric Rossby wave source pattern. The high pattern consistency only shows up for amplitudes of the Rossby wave source greater than one standard deviation (dashed line in Fig. 11a). Hence, it suggests that a Rossby wave source of a sufficient strength is needed to produce consistent teleconnection patterns. We also performed additional analysis by replacing the two reference time series of the

Rossby wave source with those of Indian Ocean and west Pacific tropical OLR (5° S– 7.5° N, 75° – 100° E and 5° S– 7.5° N, 145° – 170° E) to test more directly how tropical convection influences the pattern consistency in the extratropical regions. The results with the OLR-based time series are qualitatively similar to the Rossby wave source-based time series (results not shown). We additionally examined the Z500 pattern consistency based on MC_{RWS} and the result is shown in Fig. 11b. From Fig. 11b, it appears that the Z500 pattern consistency is largely independent of MC_{RWS} . The consistency values range from only 11% to 15%, which implies that MC_{RWS} is not a strong determinant in producing the Z500 pattern consistency in the extratropical Pacific. Overall, the result in Fig. 11 demonstrates that dipole structures of Rossby wave source across the jet can generate consistent teleconnection patterns in the extratropical Pacific while a monopole structure does not.

The results shown in Figs. 10 and 11 are based on the Rossby wave source. However, we have not explicitly looked into the specific role of the MJO in Figs. 10 and 11. Figure 12 shows the frequency with which specific MJO phases can generate a dipole structure of a Rossby wave source across the jet at a lag of 1 day (e.g., $EI_{RWS} < 0$, $WP_{RWS} > 0$ or $EI_{RWS} > 0$, $WP_{RWS} < 0$). Over 50% of MJO phase 2 and phase 3 events generate Rossby wave sources with $EI_{RWS} < 0$ and $WP_{RWS} > 0$, and MJO phases

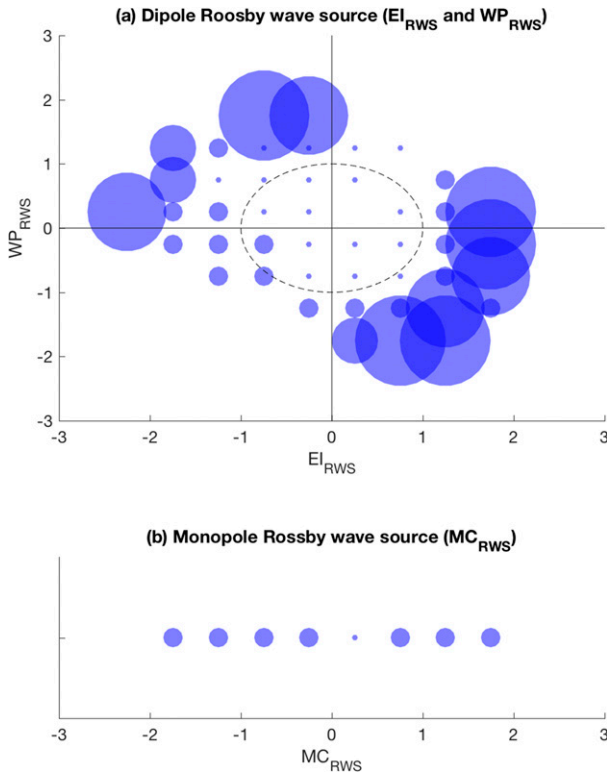


FIG. 11. The pattern consistency of 500-hPa geopotential height anomalies at a lag of 10 day in the domain of 20° – 70° N, 150° E– 120° W as a function of (a) EI_{RWS} and WP_{RWS} and (b) MC_{RWS} . The intervals of EI_{RWS} , WP_{RWS} , and MC_{RWS} are 0.5σ . Five different dot sizes from small to large correspond to the following five different pattern consistency values: 11%–13%, 13%–15%, 15%–17%, 17%–19%, and $>19\%$. If the pattern consistency is smaller than 11%, or the sample size is smaller than 30, the value is omitted.

6 and 7 have greater than 50% chance of generating a Rossby wave source with $EI_{RWS} > 0$ and $WP_{RWS} < 0$. Notably, these are also the phases showing consistent Z500 patterns at lag 10–15 in the extratropical Pacific (Fig. 1). This indicates that the MJO phases that have Rossby wave sources in the second and the fourth quadrants are more likely to generate similar teleconnections pattern due to the constructive interference of PNA-like signals. By contrast, other MJO phases (i.e., phases 1, 4, 5, and 8) with Rossby wave sources evenly distributed across the four quadrants have similar probabilities of generating PNA-like patterns and non-PNA-like patterns. This probability distribution results from the location of MJO heating. Since MJO phases 1, 4, 5, and 8 have anomalous heating located in the Maritime Continent, subtle shifts of horizontal MJO heating structure determine which Rossby wave source on opposite sides of the jet dominates the teleconnection pattern. The symmetric pattern of the Rossby wave source generated by these MJO phases is similar to a seesaw with equal weight on each side. Any

small perturbation can easily break the balance. Hence, for these phases the pattern consistency is greatly reduced due to event-to-event variability in the precise heating structure.

6. Conclusions and remarks

Heating-induced tropical–extratropical teleconnections play an important role in modulating extratropical circulation patterns and hence weather events. Since the MJO is a dominant mode of variability on intraseasonal time scales, it is intuitive to leverage information about the MJO for S2S time scale prediction in extratropical regions given the strong teleconnections produced by MJO convective heating. The major goal of this study is to examine why specific MJO phases favor a more consistent teleconnection pattern while others do not. In this study, a set of perturbed basic states or perturbed phase-dependent MJO heating distributions are applied in a linear baroclinic model (LBM) to create an ensemble, and the MJO phase-dependent consistency of teleconnection patterns across the ensemble of simulations is assessed, much as Tseng et al. (2018) assessed the pattern consistency in a hindcast ensemble. The results indicate that the consistency of the teleconnection pattern is a function of MJO phase that approximately corresponds to the geographical locations of MJO heating anomalies. Teleconnection patterns during MJO phases 2, 3, 6, and 7 are less sensitive to modest variations of the basic state and anomalous heating patterns compared to other MJO phases. An explanation for this phase-dependent pattern consistency is proposed by calculating the sign agreement of linearized Rossby wave source over different model realizations. Phases with a more dipole-like pattern of anomalous Rossby wave source on the east and west side of the Pacific jet are also the phases showing higher pattern consistency of teleconnections in both model and reanalysis. Heating location tests also demonstrate that both MJO convection in the eastern Indian Ocean and the western Pacific generate similar asymmetric Rossby wave source patterns and teleconnections in the LBM, except with opposite sign. Given the linearity of the model, this result implies that an enhanced teleconnection signal may appear for the phases with a dipole-type pattern of Indo-Pacific warm pool heating and a dipole Rossby wave source along the jet because of the constructive interference of similar teleconnection patterns. However, it also implies that other phases with less significant Z500 composite patterns may be caused by the lack of a dipole structure and, thus, more variability in the teleconnection pattern from event to event. In the last section, the relationship between the Rossby wave source on each side of the jet and the robustness of tropical–extratropical

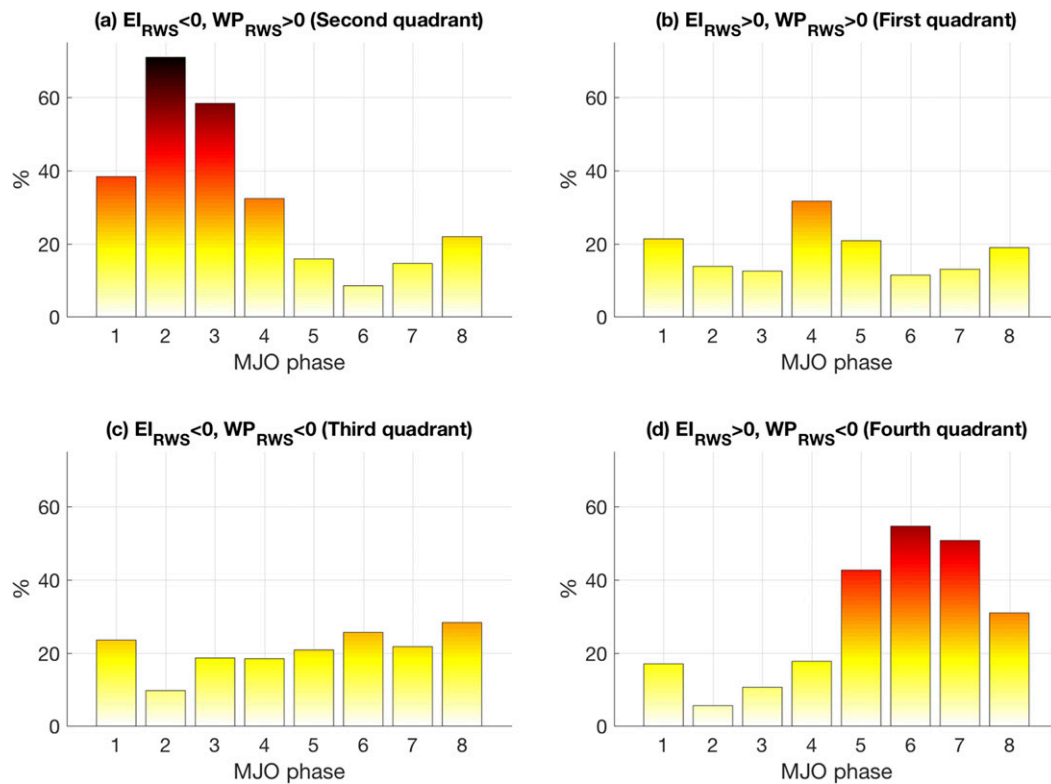


FIG. 12. The frequency that specific MJO phases generate a Rossby wave source with (a) $EI_{RWS} < 0, WP_{RWS} > 0$; (b) $EI_{RWS} > 0, WP_{RWS} > 0$; (c) $EI_{RWS} < 0, WP_{RWS} < 0$; and (d) $EI_{RWS} > 0, WP_{RWS} < 0$ within ERA-Interim.

teleconnections in reanalysis data is examined, initially without explicit consideration of the MJO. The analysis showed that an asymmetric Rossby wave source pattern zonally across the jet not only enhances the composited amplitude of Z500, but also increases the pattern consistency of Z500 over different events, as was found in the LBM. The MJO-induced teleconnection results can be regarded as a special case of this behavior.

This study gives a possible explanation for the phase-dependent pattern consistency of Z500 described in Tseng et al. (2018), who found that robust tropical–extratropical teleconnections for certain MJO phases can benefit S2S time scale weather prediction. However, a number of unanswered questions still exist. First, will the MJO phase-dependent pattern consistency change when other low-frequency variability is considered? Since other modes of climate variability (e.g., quasi-biennial oscillation or ENSO) modulate MJO activity including MJO propagation speed and convection intensity as well as the basic state, it would be interesting to examine how these modes of climate variability affect MJO phase-dependent pattern consistency. Second, the mechanisms discussed in this study are based on linear dynamics, but nonlinear feedbacks may also be important. For example, Watanabe and Jin (2004) showed that the

subtropical jet is an amplifier for tropical–extratropical teleconnections through zonal mean–eddy feedback processes. How such feedbacks influence the robustness of tropical–extratropical teleconnections is still an ongoing area of research.

The results of this study provide a compelling explanation for the MJO phase-dependent consistency of teleconnection patterns first described in Tseng et al. (2018) by invoking linear Rossby wave dynamics. This study also gives a possible explanation for why MJO phases with consistent teleconnections are also characterized by small model ensemble spreads and improved prediction skills. However, the nonlinear dynamics and interaction between physics schemes in a numerical weather forecast system are more complicated than the linearized dynamical core used in this study. Thus, relating our results to these more complex dynamical forecast systems requires additional future research.

Acknowledgments. We thank the members in BMRT group for helpful comments on the analysis. We also thank Dr. Stephanie Henderson for providing a tutorial on the LBM. This research has been conducted as part of the NOAA MAPP S2S Prediction Task Force and

supported by NOAA grant NA16OAR4310064. EDM was also supported by NSF Grant AGS-1441916.

REFERENCES

- Adames, Á. F., and D. Kim, 2016: The MJO as a dispersive, convectively coupled moisture wave: Theory and observations. *J. Atmos. Sci.*, **73**, 913–941, <https://doi.org/10.1175/JAS-D-15-0170.1>.
- Bjerknes, J., 1969: Atmospheric teleconnections from the equatorial Pacific. *Mon. Wea. Rev.*, **97**, 163–172, [https://doi.org/10.1175/1520-0493\(1969\)097<0163:ATFTEP>2.3.CO;2](https://doi.org/10.1175/1520-0493(1969)097<0163:ATFTEP>2.3.CO;2).
- Black, R. X., 1997: Deducing anomalous wave source regions during the life cycles of persistent flow anomalies. *J. Atmos. Sci.*, **54**, 895–907, [https://doi.org/10.1175/1520-0469\(1997\)054<0895:DAWSRD>2.0.CO;2](https://doi.org/10.1175/1520-0469(1997)054<0895:DAWSRD>2.0.CO;2).
- Dee, D. P., and Coauthors, 2011: The ERA-Interim reanalysis: Configuration and performance of the data assimilation system. *Quart. J. Roy. Meteor. Soc.*, **137**, 553–597, <https://doi.org/10.1002/qj.828>.
- Ferranti, L., T. N. Palmer, F. Molteni, and E. Klinker, 1990: Tropical–extratropical interaction associated with the 30–60 day oscillation and its impact on medium and extended range prediction. *J. Atmos. Sci.*, **47**, 2177–2199, [https://doi.org/10.1175/1520-0469\(1990\)047<2177:TEIAWT>2.0.CO;2](https://doi.org/10.1175/1520-0469(1990)047<2177:TEIAWT>2.0.CO;2).
- Gill, A. E., 1980: Some simple solutions for heat-induced tropical circulation. *Quart. J. Roy. Meteor. Soc.*, **106**, 447–462, <https://doi.org/10.1002/qj.49710644905>.
- Hamill, T. M., and G. N. Kiladis, 2014: Skill of the MJO and Northern Hemisphere blocking in GEFs medium-range reforecasts. *Mon. Wea. Rev.*, **142**, 868–885, <https://doi.org/10.1175/MWR-D-13-00199.1>.
- Held, I. M., S. W. Lyons, and S. Nigam, 1988: Transients and the extratropical response to El Niño. *J. Atmos. Sci.*, **45**, 163–174, [https://doi.org/10.1175/1520-0469\(1988\)045<0163:TATERT>2.0.CO;2](https://doi.org/10.1175/1520-0469(1988)045<0163:TATERT>2.0.CO;2).
- Henderson, S. A., E. D. Maloney, and E. A. Barnes, 2016: The influence of the Madden–Julian oscillation on Northern Hemisphere winter blocking. *J. Climate*, **29**, 4597–4616, <https://doi.org/10.1175/JCLI-D-15-0502.1>.
- , —, and S.-W. Son, 2017: The impact of the basic state and MJO representation in general circulation models. *J. Climate*, **30**, 4567–4587, <https://doi.org/10.1175/JCLI-D-16-0789.1>.
- Hendon, H. H., C. Zhang, and J. D. Glick, 1999: Interannual variation of the Madden–Julian oscillation during austral summer. *J. Climate*, **12**, 2538–2550, [https://doi.org/10.1175/1520-0442\(1999\)012<2538:IVOTMJ>2.0.CO;2](https://doi.org/10.1175/1520-0442(1999)012<2538:IVOTMJ>2.0.CO;2).
- Hirota, N., and M. Takahashi, 2012: A tripolar pattern as an internal mode of the East Asian summer monsoon. *Climate Dyn.*, **39**, 2219–2238, <https://doi.org/10.1007/s00382-012-1416-y>.
- Hoskins, B. J., and D. J. Karoly, 1981: The steady linear response of a spherical atmosphere to thermal and orographic forcing. *J. Atmos. Sci.*, **38**, 1179–1196, [https://doi.org/10.1175/1520-0469\(1981\)038<1179:TSLROA>2.0.CO;2](https://doi.org/10.1175/1520-0469(1981)038<1179:TSLROA>2.0.CO;2).
- Hsu, H.-H., 1996: Global view of the intraseasonal oscillation during northern winter. *J. Climate*, **9**, 2386–2406, [https://doi.org/10.1175/1520-0442\(1996\)009<2386:GVOTIO>2.0.CO;2](https://doi.org/10.1175/1520-0442(1996)009<2386:GVOTIO>2.0.CO;2).
- Jin, F.-F., L.-L. Pan, and M. Watanabe, 2006: Dynamics of synoptic eddy and low-frequency flow interaction. Part I: A linear closure. *J. Atmos. Sci.*, **63**, 1677–1694, <https://doi.org/10.1175/JAS3715.1>.
- Kiladis, G. N., J. Dias, K. H. Straub, M. C. Wheeler, S. N. Tulich, K. Kikuchi, K. M. Weickmann, and M. J. Ventrice, 2014: A comparison of OLR and circulation-based indices for tracking the MJO. *Mon. Wea. Rev.*, **142**, 1697–1715, <https://doi.org/10.1175/MWR-D-13-00301.1>.
- Kim, J.-H., C.-H. Ho, H.-S. Kim, C.-H. Sui, and S. K. Park, 2008: Systematic variation of summertime tropical cyclone activity in the western North Pacific in relation to the Madden–Julian oscillation. *J. Climate*, **21**, 1171–1191, <https://doi.org/10.1175/2007JCLI1493.1>.
- Kimoto, M., F.-F. Jin, M. Watanabe, and N. Yasutomi, 2001: Zonal–eddy coupling and a neutral mode theory for the Arctic Oscillation. *Geophys. Res. Lett.*, **28**, 737–740, <https://doi.org/10.1029/2000GL012377>.
- Lawrence, D. M., and P. J. Webster, 2002: The boreal summer intraseasonal oscillation: Relationship between northward and eastward movement of convection. *J. Atmos. Sci.*, **59**, 1593–1606, [https://doi.org/10.1175/1520-0469\(2002\)059<1593:TBSIOR>2.0.CO;2](https://doi.org/10.1175/1520-0469(2002)059<1593:TBSIOR>2.0.CO;2).
- Liebmann, B., H. H. Hendon, and J. D. Glick, 1994: The relationship between tropical cyclones of the western Pacific and Indian Oceans and the Madden–Julian oscillation. *J. Meteor. Soc. Japan*, **72**, 401–412, https://doi.org/10.2151/jmsj1965.72.3_401.
- Madden, R. A., and P. R. Julian, 1971: Detection of a 40–50 day oscillation in the zonal wind in the tropical Pacific. *J. Atmos. Sci.*, **28**, 702–708, [https://doi.org/10.1175/1520-0469\(1971\)028<0702:DOADOI>2.0.CO;2](https://doi.org/10.1175/1520-0469(1971)028<0702:DOADOI>2.0.CO;2).
- Maloney, E. D., and D. L. Hartmann, 2000: Modulation of hurricane activity in the Gulf of Mexico by the Madden–Julian oscillation. *Science*, **287**, 2002–2004, <https://doi.org/10.1126/science.287.5460.2002>.
- Matthews, A. J., B. J. Hoskins, and M. Masutani, 2004: The global response to tropical heating in the Madden–Julian oscillation during the northern winter. *Quart. J. Roy. Meteor. Soc.*, **130**, 1991–2011, <https://doi.org/10.1256/qj.02.123>.
- Mori, M., and M. Watanabe, 2008: The growth and triggering mechanisms of the PNA: A MJO–PNA coherence. *J. Meteor. Soc. Japan*, **86**, 213–236, <https://doi.org/10.2151/jmsj.86.213>.
- Mundhenk, B. D., E. A. Barnes, and E. D. Maloney, 2016: All-season climatology and variability of atmospheric river frequencies over the North Pacific. *J. Climate*, **29**, 4885–4903, <https://doi.org/10.1175/JCLI-D-15-0655.1>.
- Sardeshmukh, P.-D., and B.-J. Hoskins, 1988: The generation of global rotational flow by steady idealized tropical divergence. *J. Atmos. Sci.*, **45**, 1228–1251, [https://doi.org/10.1175/1520-0469\(1988\)045<1228:TGOGRF>2.0.CO;2](https://doi.org/10.1175/1520-0469(1988)045<1228:TGOGRF>2.0.CO;2).
- Seo, K.-H., and H.-J. Lee, 2017: Mechanisms for a PNA-like teleconnection pattern in response to the MJO. *J. Atmos. Sci.*, **74**, 1767–1781, <https://doi.org/10.1175/JAS-D-16-0343.1>.
- Simmons, A. J., J. M. Wallace, and G. W. Branstator, 1983: Barotropic wave propagation and instability, and atmospheric teleconnection patterns. *J. Atmos. Sci.*, **40**, 1363–1392, [https://doi.org/10.1175/1520-0469\(1983\)040<1363:BWPAIA>2.0.CO;2](https://doi.org/10.1175/1520-0469(1983)040<1363:BWPAIA>2.0.CO;2).
- Sui, C.-H., and K.-M. Lau, 1992: Multiscale phenomena in the tropical atmosphere over the western Pacific. *Mon. Wea. Rev.*, **120**, 407–430, [https://doi.org/10.1175/1520-0493\(1992\)120<0407:MPITTA>2.0.CO;2](https://doi.org/10.1175/1520-0493(1992)120<0407:MPITTA>2.0.CO;2).
- Tseng, K.-C., E. A. Barnes, and E. D. Maloney, 2018: Prediction of the midlatitude response to strong Madden–Julian oscillation events on S2S timescales. *Geophys. Res. Lett.*, **45**, 463–470, <https://doi.org/10.1002/2017GL075734>.
- Vitart, F., 2017: Madden–Julian oscillation prediction and teleconnections in the S2S database: MJO prediction and teleconnections in the S2S database. *Quart. J. Roy. Meteor. Soc.*, **143**, 2210–2220, <https://doi.org/10.1002/qj.3079>.

- Watanabe, M., and M. Kimoto, 2000: Atmosphere–ocean thermal coupling in the North Atlantic: A positive feedback. *Quart. J. Roy. Meteor. Soc.*, **126**, 3343–3369, <https://doi.org/10.1002/qj.49712657017>.
- , and F.-F. Jin, 2004: Dynamical prototype of the Arctic Oscillation as Revealed by a neutral singular vector. *J. Climate*, **17**, 2119–2138, [https://doi.org/10.1175/1520-0442\(2004\)017<2119:DPOTAO>2.0.CO;2](https://doi.org/10.1175/1520-0442(2004)017<2119:DPOTAO>2.0.CO;2).
- Yanai, M., S. Esbensen, and J.-H. Chu, 1973: Determination of bulk properties of tropical cloud clusters from large-scale heat and moisture budgets. *J. Atmos. Sci.*, **30**, 611–627, [https://doi.org/10.1175/1520-0469\(1973\)030<0611:DOBPOT>2.0.CO;2](https://doi.org/10.1175/1520-0469(1973)030<0611:DOBPOT>2.0.CO;2).
- Yoo, C., S. Lee, and S. B. Feldstein, 2012: Mechanisms of Arctic surface air temperature change in response to the Madden–Julian oscillation. *J. Climate*, **25**, 5777–5790, <https://doi.org/10.1175/JCLI-D-11-00566.1>.